Applied Surface Science 473 (2019) 194–202

Contents lists available at ScienceDirect

Applied Surface Science

journal homepage: www.elsevier.com/locate/apsusc

Full Length Article

Multiple resistive switching behaviours of $CH_3NH_3PbI_3$ perovskite film with different metal electrodes

Gregory Thien Soon How[a], Noor Azrina Talik[a,*], Yap Boon Kar[b,c], Hideki Nakajima[d], Sarayut Tunmee[d], Goh Boon Tong[a,*]

[a] *Low Dimensional Materials Research Centre, Department of Physics, Faculty of Science, University of Malaya, 50603 Kuala Lumpur, Malaysia*
[b] *Electronic and Communications Department, College of Engineering, Universiti Tenaga Nasional, 43000 Kajang, Selangor, Malaysia*
[c] *International School of Advanced Materials, South China University of Technology, 381 Wushan Road, Tianhe District, Guangzhou, Guangdong, PR China*
[d] *Synchrotron Light Research Institute (SLRI), Nakhon Ratchasima 30000, Thailand*

ARTICLE INFO

Keywords:
Organic-inorganic perovskite
Resistive switching
Charge trapping
Filamentary conduction

ABSTRACT

The utilization of defects in organic-inorganic hybrid perovskite materials such as $CH_3NH_3PbI_3$ is beneficial for memory applications. In this work, a simple $CH_3NH_3PbI_3$ memory device with various commonly used electrodes such as aluminium (Al), silver (Ag), and gold (Au) yielded different switching behaviours. Using Al in ITO/$CH_3NH_3PbI_3$/Al device reveals Resistive Random Access Memory (ReRAM) behaviour with a SET voltage of 4.5 V and can be RESET by applying a negative sweep voltage above 1.3 V due to the formation of iodide vacancy filament. Interestingly, by using Ag and Au cathodes to replace Al, yielded Write-Once-Read-Many (WORM) resistive switching characteristics. The conversion process from OFF to ON occur at around 4.7 V and 4.0 V for Ag and Au, respectively. The “shorting effect” remains even though a reverse voltage was applied indicating data retention. These fabricated devices could contribute to further understanding of selecting the right electrodes and open up new possibility of studies in the direction of resistive switching memory applications.

1. Introduction

Memory applications play an important role in today’s fast paced evolution of digital technology. Next generation non-volatile memory device research has sparked a great acceleration to obtain high performance memory devices. Among organic-inorganic hybrid materials perovskite materials have captured great interest in various applications owing to their unique properties of long charge diffusion length, strong optical absorption, non-linear dielectric behaviour, and high magnetic/electronic properties [1–6]. Perovskites structures have a general stoichiometry of ABX_3 with A and B as different size cations and X as anion [7]. A commonly used perovskite material namely $CH_3NH_3PbI_3$ has been employed in various application such as solar cells [8–11], photodetectors [12–14], supercapacitors [15], LEDs [16,17], as well as memory devices [18–20].

Amongst popular memory applications, Resistive Random Access Memory (ReRAM) oversees a high demand in portable electronic devices due to the advantages of high memory density, low power consumption, simple structure, and the cost-effectiveness in fabricating the devices [21–24]. In addition to that, ReRAM exhibits a favourable switching behaviour between high and low resistive states which combines the advantages for both RAM and flash memory. On the other hand, a Write-Once-Read-Many (WORM) resistive switching memory application demonstrates irreversible memory-switching to a high-conducting state even if a reverse bias is applied [25]. This type of application is useful in conventional programmable read-only memory devices or the commonly used DVD-R and CD-R media. To date, numbers of publications had reported on the use of $CH_3NH_3PbI_3$ in resistive switching devices. For example Gu et al. reported on the flexible ReRAM Au/$CH_3NH_3PbI_3$/ITO memory device with very low operation voltage by taking the advantage of the vacancy defects in $CH_3NH_3PbI_3$ [22]. Liu et al. published their work on reprogrammable ITO/PMMA/$CH_3NH_3PbI_3$/PMMA/Ag device with ON/OFF ratio around $\sim 10^3$ and ReRAM memory characteristics [19]. While Wang et al. reported non-volatile WORM memory behaviour based on their ITO/$CH_3NH_3PbI_3$:PVK/Al structure [26]. Albeit numbers of reports demonstrating ReRAM or WORM memory characteristics using $CH_3NH_3PbI_3$ layers with different metal contacts [19,21,22,27], to author’s best knowledge, there is none of these studies had done a direct comparison of different metal cathode effect on the $CH_3NH_3PbI_3$ based memory device. The lack of deep understanding on the effect of various metals, such as Au, Ag, and Al as metal contacts still needs to be

---

* Corresponding authors.
E-mail addresses: azrinatalik@um.edu.my (N.A. Talik), gohbt@um.edu.my (B.T. Goh).

https://doi.org/10.1016/j.apsusc.2018.12.124
Received 23 October 2018; Received in revised form 7 December 2018; Accepted 13 December 2018

explored. Hence, in this work, we reported a direct comparison on the effect of different metal towards the device memory behaviour. In this paper, a simple device structure of ITO/$CH_3NH_3PbI_3$/X where X = Al, Ag, Au were fabricated. It was observed that thermal evaporation of different metal contacts on the $CH_3NH_3PbI_3$ layers demonstrated different memory behaviours of ReRAM and WORM.

2. Materials and methods

2.1. Materials

Chemical reagents such as *N,N*-dimethylformamide (DMF), lead(II) iodide (PbI_2), silver wire (Ag, 99.99%) were purchased from Merck. Isopropyl alcohol (IPA) for cleaning was obtained from Systerm Chemicals while Methylammonium iodide (MAI) was received from Solaronix. Chlorobenzene (CB) was supplied by Friendemann Schmidt. Gold wires (Au, 99.99%) and Aluminium wire (Al, 99.9999%) were purchased from Kurt J. Lesker. All chemical reagents were used as received without further purification.

2.2. $CH_3NH_3PbI_3$ memory device preparation

Pre-patterned ITO-coated glass substrates were cleaned in an ultrasonic bath in acetone, isopropyl alcohol and deionized water in sequence, and then were dry-purged using nitrogen flow. The $CH_3NH_3PbI_3$ layers with an average thickness of ~300 nm were prepared via two-step spin coating method. First, 462 mg of PbI_2 was dissolved in 1 ml of DMF at 70 °C on a hot plate overnight. The PbI_2 solution was then spin coated onto the ITO substrate at 3000 rpm for 30 s and then immediately heated at 100 °C for 10 min. Next, the PbI_2 coated substrate was dipped in 10 mg/ml MAI in IPA for 40 s to form $CH_3NH_3PbI_3$ layer. Then, chlorobenzene was dropped on the $CH_3NH_3PbI_3$ layer, spin coated for 30 s and subsequently annealed at 100 °C. Finally, metal contacts (Al, Ag, Au) were thermally evaporated on top of the $CH_3NH_3PbI_3$ layer at a thickness of approximately 100 nm. The whole process of the device fabrication was executed under inert conditions in a glove box.

2.3. Characterization techniques

Perovskite structure were analyzed using X-ray Diffraction (XRD) pattern using Panalytical Empyrean XRD, while Field Emission Scanning Electron Microscope (FESEM) images of the perovskite films were acquired using Hitachi SU8230 Cold Field UHR FESEM. The optical characteristics of the films such as emission peak and band gap were measured via photoluminescence (PL) spectra with an excitation wavelength of 325 nm and PerkinElmer LAMBDA 750 UV/Vis/NIR spectrophotometer respectively. Surface elemental analysis and band alignment were also performed using Ultraviolet Photoelectron Spectroscopy and X-ray Photoelectron Spectroscopy (UPS/XPS) with photon energy of 600 eV and 39.5 eV respectively, using gold metal, Au as reference. The UPS/XPS measurements were carried out in beamline no. 3.2 at Synchrotron Light Research Institute, Thailand. Finally, the Current-Voltage (*I-V*) characteristics of the fabricated devices were measured with a dual-channel system sourcemeter (Keithley 2612B). Bias voltage was applied to the top metal electrode with respect to ITO for all measurements.

3. Results & discussion

3.1. Optical, structural and surface characteristics of $CH_3NH_3PbI_3$ perovskite

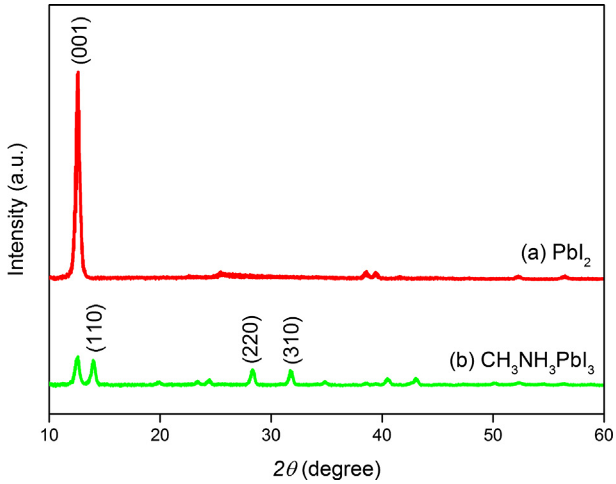

Fig. 1. XRD pattern of (a) PbI_2 and (b) $CH_3NH_3PbI_3$ perovskite films.

The formation of $CH_3NH_3PbI_3$ perovskite originated from PbI_2 film using a two-step dipping method is shown in XRD spectra in Fig. 1. Originally, pure PbI_2 film shows to exhibit a distinct peak at $2\theta = 12.53°$ position or (0 0 1) plane (Fig. 1a), referring to the PbI_2 hexagonal crystal structure [28]. After PbI_2 was converted to $CH_3NH_3PbI_3$ perovskite, the (0 0 1) peak is observed to reduce, simultaneously, new peaks at $2\theta = 14.01°$, 28.33°, 31.77° corresponding to (1 1 0), (2 2 0), and (3 1 0) crystal planes emerged (Fig. 1b) [29,30]. This indicates the formation of tetragonal perovskite structure [18]. Nevertheless, it can be seen that there was still some remnants of PbI_2 in the $CH_3NH_3PbI_3$ perovskite ($2\theta = 12.53°$), which can be further reduced by increasing the dipping time [31]. However, it is reported that $CH_3NH_3PbI_3$ film formed by longer dipping time (up to 120 mins) yielded thicker films and rougher surface that will increase the presence of voids and pinholes [32]. The surface morphology of both films was further investigated with FESEM.

FESEM images in Fig. 2a and b show that the spin coated PbI_2 films yielded a porous and loose structure which implies a good film formation to be converted into $CH_3NH_3PbI_3$ perovskite [33]. Although some pinholes were observed on the PbI_2 films, the converted $CH_3NH_3PbI_3$ perovskite in Fig. 2c and d reveal an excellent and dense coverage of perovskite crystals when methylammonium iodide (MAI) was infused into the PbI_2 films. Moreover, the film shows an even distribution of homogenous $CH_3NH_3PbI_3$ perovskite crystals formed in this work, which is quite in good agreement with that reported solution processed $CH_3NH_3PbI_3$ perovskites [34,35]. The elemental analysis using XPS was then carried out to investigate the properties of the perovskite film prepared.

Fig. 3 depicts the full-scan XPS spectra of $CH_3NH_3PbI_3$ perovskite spin coated on ITO substrate. Common elements of $CH_3NH_3PbI_3$ were detected in the wide scan spectra shown in Fig. 3(a) including Pb*4f*, I*3d*, C*1s*, as well as N*1s* [36]. The atomic ratio of C : N : Pb : I estimated in the $CH_3NH_3PbI_3$ perovskite from the narrow scan shown in Fig. 3b–e and taken into account the background spectra are 1.15 : 1.12 : 1.00 : 2.86, which is consistent with the reported $CH_3NH_3PbI_3$ perovskite structure [37]. Fig. 3(b) reveals the doublet peaks of I $3d_{3/2}$ and I $3d_{5/2}$ at 631.1 eV and 619.1 eV in which I $3d_{5/2}$ corresponds to the triiodide ion I^{3-} in $CH_3NH_3PbI_3$ film [38]. In addition to that, the narrow scan for Pb *4f* (Fig. 3c) shows the spin-orbit splitting of the *f* orbital in which two distinct peaks were assigned to Pb $4f_{7/2}$ and Pb $4f_{5/2}$. The binding energy of Pb $4f_{7/2}$ is in good agreement corresponding to the Pb^{2+} in the $CH_3NH_3PbI_3$ perovskite [39,40]. In Fig. 3d, the C *1s* spectrum fitting reveals only one distinct peak which is probably contributed by the methyl carbons sourced from the methylammonium ions [38].

Fig. 4 shows the optical properties of pure PbI_2 and its conversion into $CH_3NH_3PbI_3$ perovskite. A typical absorption edge for PbI_2 at about 500 nm was observed in Fig. 4a. The absence of the absorption spectra above 500 nm might due to the interference patterns indicating a smooth PbI_2 layer formed [30]. When the PbI_2 film was converted into

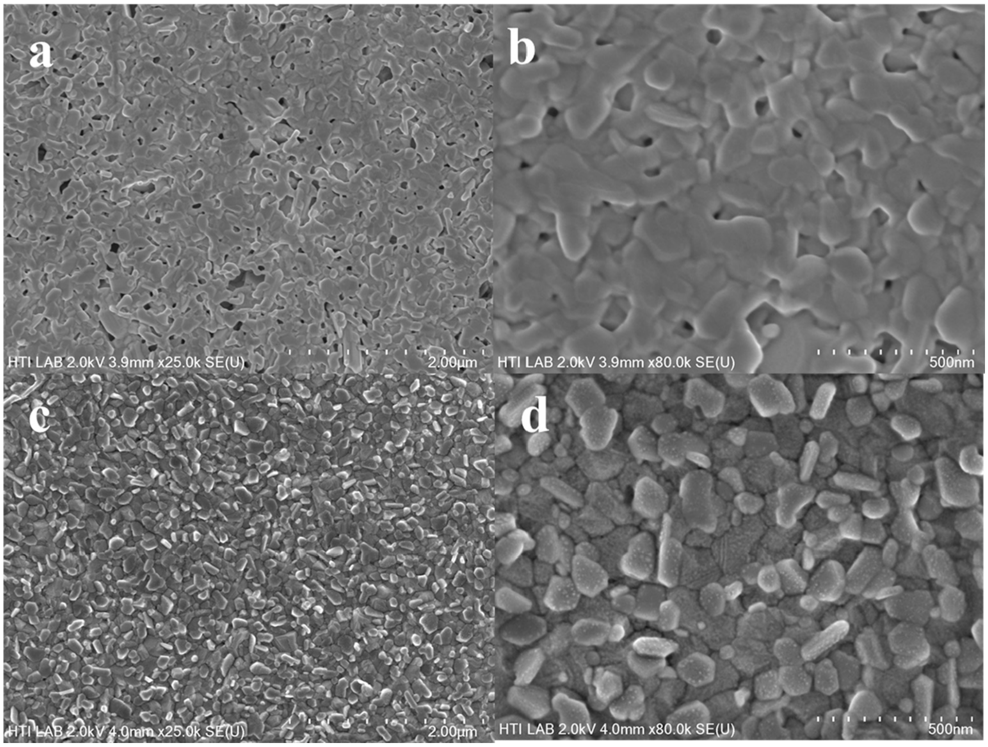

Fig. 2. FESEM micrographs of PbI_2 at (a) low (2.0 μm) and (b) high magnifications (500 nm) and $CH_3NH_3PbI_3$ perovskite morphology at (c) low (2.0 μm) and (d) high magnifications (500 nm).

$CH_3NH_3PbI_3$ perovskite layer, a strong absorption spectra in the range of 400 nm to 800 nm with an absorption edge of 760 nm was observed. This absorption characteristics is consistent with previous literature studies reporting the properties of $CH_3NH_3PbI_3$ perovskite [33,41].

In Fig. 4b, the PL spectra in the PbI_2 substrate show an emission peak at about 535 nm. When the PbI_2 substrate was dipped into the MAI solution, this emission peak diminishes and a new emission peak emerges at 776 nm indicating the full conversion of PbI_2 to $CH_3NH_3PbI_3$. This can be attributed to the recombination of the near band-to-band [42]. A simple way to observe a change in $CH_3NH_3PbI_3$ conversion is shown in Fig. 4c. It is commonly reported that the initial yellowish PbI_2 films spin coated on the substrate would be converted into a dark brown shiny appearance when a conversion of PbI_2 to $CH_3NH_3PbI_3$ perovskite is complete. To further analyze the synthesized $CH_3NH_3PbI_3$ perovskite characteristics, the surface band alignment of the film was characterized via UPS measurement shown in Fig. 5.

The wide scan of $CH_3NH_3PbI_3$ perovskite spin coated on ITO substrate is shown in Fig. 5a. In order to measure the Highest Occupied Molecular Orbital (HOMO) and work function (Φ) of the film, the narrow scan with linear extrapolation of low energy cut-off region (Fig. 5b), and high energy region (Fig. 5c) were carried out. By aligning the low energy spectrum to the Au Fermi level (E_F), the HOMO level of the $CH_3NH_3PbI_3$ perovskite determined from the intercept was calculated to be 1.42 eV (Fig. 5b). Using the same method, the work function of the film was calculated to be 4.1 eV (Fig. 5c). In order to obtain the band gap (E_g), a Tauc plot; $(\alpha h\nu)^2$ against band gap energy was plotted in Fig. 5d, where α is the optical absorption coefficient, and $h\nu$ is the incident photo energy[43]. Linear extrapolation from the graph yielded the band gap of $CH_3NH_3PbI_3$ perovskite to be 1.54 eV. This value is consistent with reported solution processed $CH_3NH_3PbI_3$ perovskite studies [44,45]. From E_g and work function values, the ionization energy (IE) was calculated to be 5.52 eV. The schematic energy level diagram of $CH_3NH_3PbI_3$ perovskite spin coated on ITO (work function is adapted from [38]) is illustrated in Fig. 5(e). The values calculated in this work agrees quite well with the reports on $CH_3NH_3PbI_3$ perovskite [46,47]. The synthesized perovskite were then adapted in the memory application structure to observe the characters tics of the device.

3.2. ReRAM memory behaviour in ITO/$CH_3NH_3PbI_3$/Al device

Fig. 6a shows current-voltage characteristics of ITO/$CH_3NH_3PbI_3$/Al memory device structure. A typical ReRaM behaviour pattern was observed when voltage was applied in the sequence of: 0 V to +8 V, +8 V to 0 V, 0 V to −8 V, and −8 V to 0 V. During initial voltage sweep from 0 to +8 V, an abrupt increase of current was observed at about 4.7 V indicating the change from High Resistance State (HRS) to Low Resistance State (LRS), or known at the SET process [18]. Similarly, when a reverse potential was applied from 0 V to −8 V, a current drop was observed at about −1.3 V indicating the transition from LRS to HRS, or known as the RESET process. This SET-RESET process was observed when the experiment was repeated continuously for multiple cycles revealing a standard resistive switching effect application. It is proposed that the charge trapping causes this memory effect to take place in the $CH_3NH_3PbI_3$ perovskite layer [22,48].

To further explain the mechanism that causes the ReRaM effect in the ITO/$CH_3NH_3PbI_3$/Al memory device, the graph of Log I vs Log V was plotted (Fig. 6b). When a positive voltage was swept across the device, a steady increase in current was observed (ohmic conduction, n = ~1.36) indicating the thermally generated carriers were larger in number as compared to the injected carriers [49]. The traps were then partially filled until to about 4.7 V, the abrupt increase of current reveals the traps have been fully filled and followed a Space-Charge-Limited-Conduction mechanism (SCLC, n = ~1.87). Since SCLC mechanism was observed, it is proposed that the defects in the perovskite layer become the trapping sites [50]. There are few types of vacancies found in $CH_3NH_3PbI_3$ perovskite such as donor vacancy ($V_I^{\bullet}$), acceptor vacancies ($V_{MA.}^{'}$ $V_{Pb}^{''}$) and vacancy-mediated diffusion [51,52]. In terms of activation energies, $V_{MA.}^{'}$ and $V_{Pb}^{''}$ are higher at ~0.8 eV and ~0.5 eV, respectively while $V_I^{\bullet}$ have a very low activation energy of ~0.1 eV. Hence, in this work, we assume that due to the lower

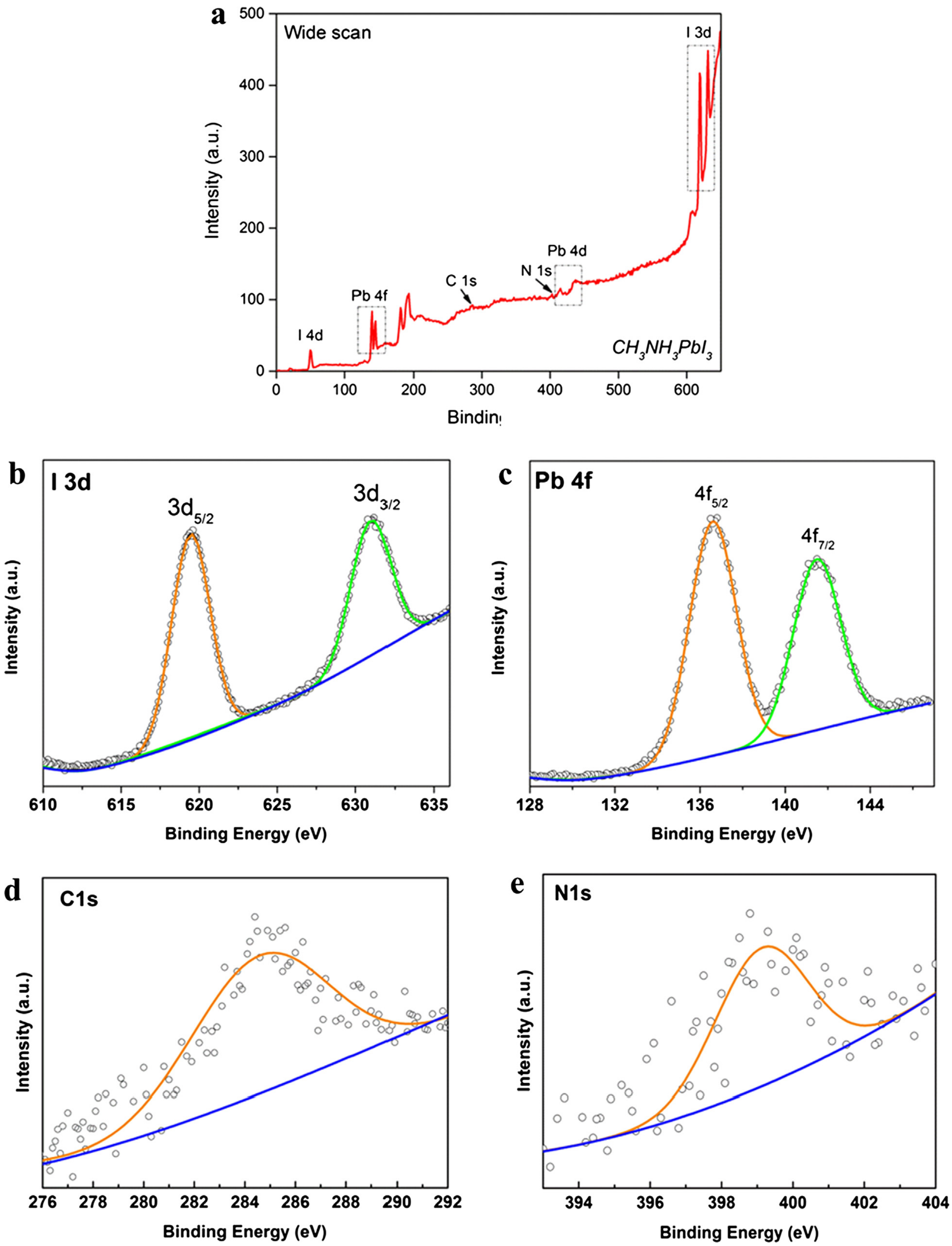

Fig. 3. XPS spectra of (a) wide scan of $CH_3NH_3PbI_3$ perovskite, (b) I 3d of $CH_3NH_3PbI_3$ perovskite, (c) Pb 4f of $CH_3NH_3PbI_3$ perovskite, (d) C 1s of $CH_3NH_3PbI_3$ perovskite, and (e) N 1s of $CH_3NH_3PbI_3$ perovskite.

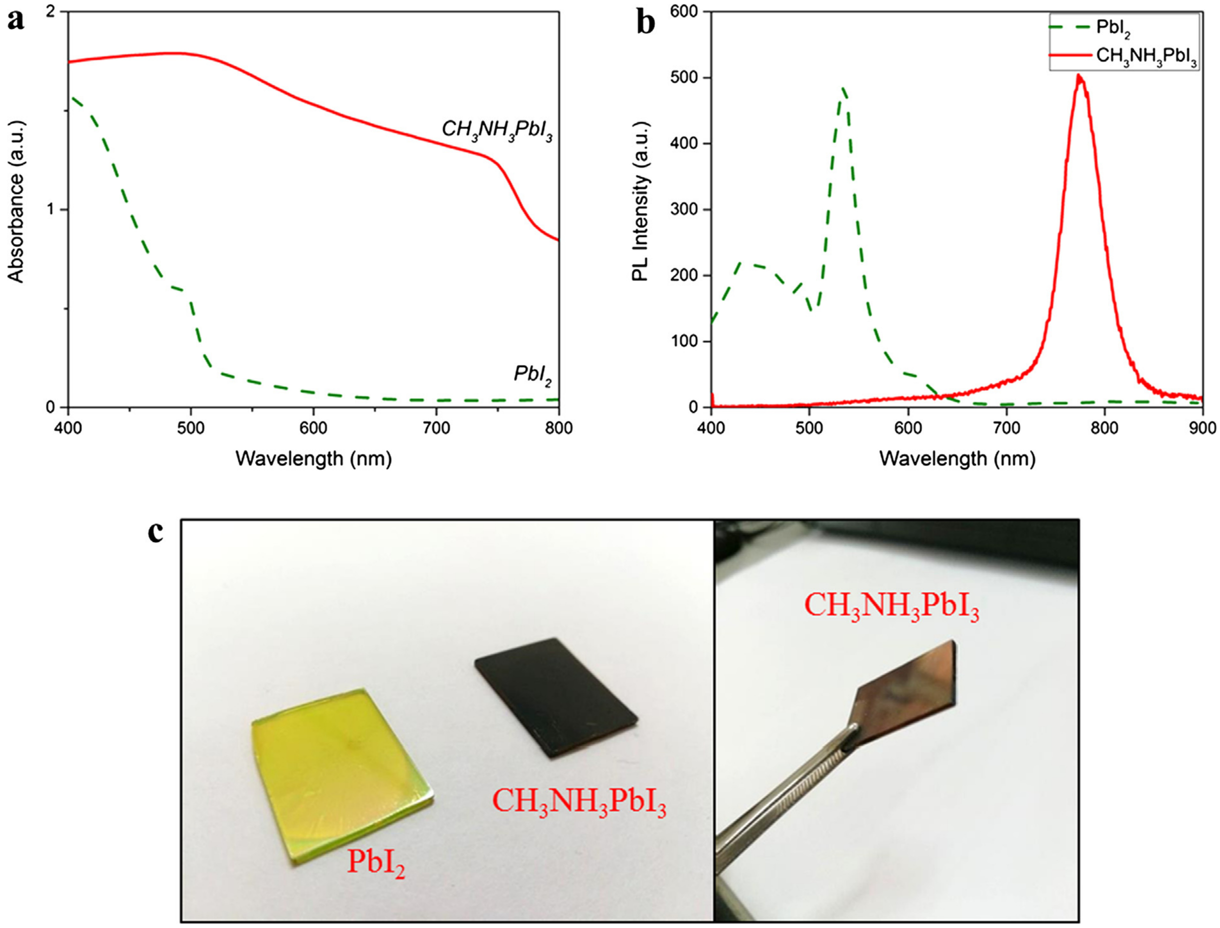

Fig. 4. (a) UV–Vis spectra of PbI_2 and $CH_3NH_3PbI_3$, (b) PL spectra of PbI_2 and $CH_3NH_3PbI_3$ perovskite, and (c) spin coated films of PbI_2 and $CH_3NH_3PbI_3$ perovskite film.

activation energy of $V_I^{\bullet}$, the positively charged iodide vacancies drift towards ITO and recombined with electrons [53]. As the voltage increased, more iodide vacancies gathered at the ITO electrode and formed an iodide vacancy filament (Fig. 6c). The charge traps were filled over time, and when the traps were fully filled, electrons could then hop trap-to-trap. To reverse this process from SET to RESET, a negative bias was applied causing the conduction path to be ruptured and electrons to be detrapped [22]. In this case, applying a reverse bias above 1.3 V is sufficient to RESET the device. Through this, the reversible process of SET-RESET yielded ReRaM characteristic in the ITO/$CH_3NH_3PbI_3$/Al device structure.

3.3. Memory behaviour in ITO/$CH_3NH_3PbI_3$/Ag and ITO/$CH_3NH_3PbI_3$/Au devices

Interestingly, when the metal contact was changed from Al to Ag, the ReRAM behaviours diminished. Instead, WORM behaviour was observed whereby the change from HRS to LRS was permanent and irreversible as shown in Fig. 7a. When a positive voltage was sweep from 0 to 10 V, the current increased steadily with voltage until at 4.7 V, an abrupt jump of current was observed. This indicates the change from HRS to LRS or also known as from OFF state to ON state. When a reverse bias voltage was applied, the state remains ON throughout the sweep range. Even though the sweep was carried up to multiple cycles, it still remained at a permanent ON state. Through this, a typical non-volatile WORM memory behaviour was observed in which the ITO/$CH_3NH_3PbI_3$/Ag device retained its data permanently.

It is suggested that the WORM memory behaviour in ITO/$CH_3NH_3PbI_3$/Ag memory device is attributed to charge trapping and filamentary conduction [26,27]. The charge traps were filled when the voltage sweep increases until all traps was filled, causing an abrupt increased of current at 4.7 V. Since it is known that charge carriers flows along the lowest resistance pathway, this filling of charge traps would also result in filamentary conduction. This abrupt increased of current could be due to the connection of top to bottom electrodes through the conductive filament by diffusion of Ag [27]. The Ag filament pathway would create a 'shorting' effect (Fig. 7c) between the ITO and Ag interfaces as well as resistive switching behaviour. When, a reverse potential was applied, the conduction pathway did not diminish but remained in LRS which is suitable for permanent data storage applications. The diffusion of Ag into the $CH_3NH_3PbI_3$ perovskite layer prevents the rupture of Ag filament unless higher sweep voltage is applied but causing the memory device to be damaged [27]. Hence, within the operating voltage window, the memory device exhibits WORM memory characteristics.

Similarly, when Ag was replaced with Au, a typical WORM behaviour is noticeable in Fig. 7b. When voltage was swept across the ITO/$CH_3NH_3PbI_3$/Au memory device, the current was also increased. The switch from HRS to LRS occurred at 4 V when an abrupt increased of current occurs. The compliance current of the memory device was set at 100 mA to prevent the device from overheating and damage. This process was also irreversible when a reverse bias voltage was applied on the ITO/$CH_3NH_3PbI_3$/Au memory device. The electrons cannot be removed from the charge traps even though the reverse voltage was swept across the device. Hence, WORM behaviour property was demonstrated when Au cathode was used in ITO/$CH_3NH_3PbI_3$/Au memory device. Overall, Au contact is much stable than Al or Ag when voltage swept across as Au is much more inert and react slower than Al or Ag.

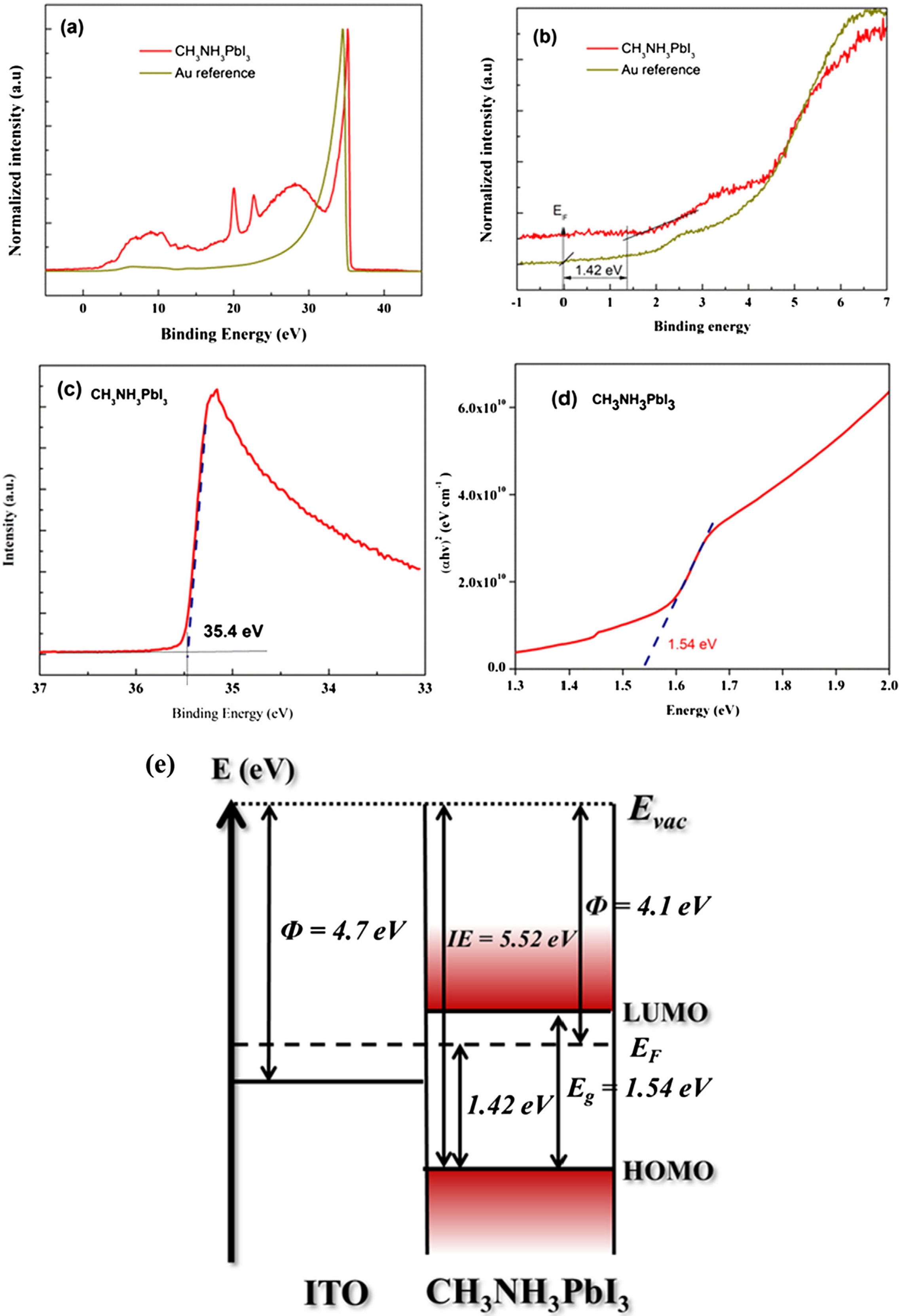

Fig. 5. (a) Wide scan UPS spectra of Au reference and $CH_3NH_3PbI_3$ perovskite, (b) low energy cut-off region of Au reference and $CH_3NH_3PbI_3$ perovskite, (c) high energy region of $CH_3NH_3PbI_3$ perovskite, (d) Tauc plot obtained from UV–Vis spectra of $CH_3NH_3PbI_3$ perovskite, and (e) energy level diagram of $CH_3NH_3PbI_3$ perovskite spin coated on ITO substrate.

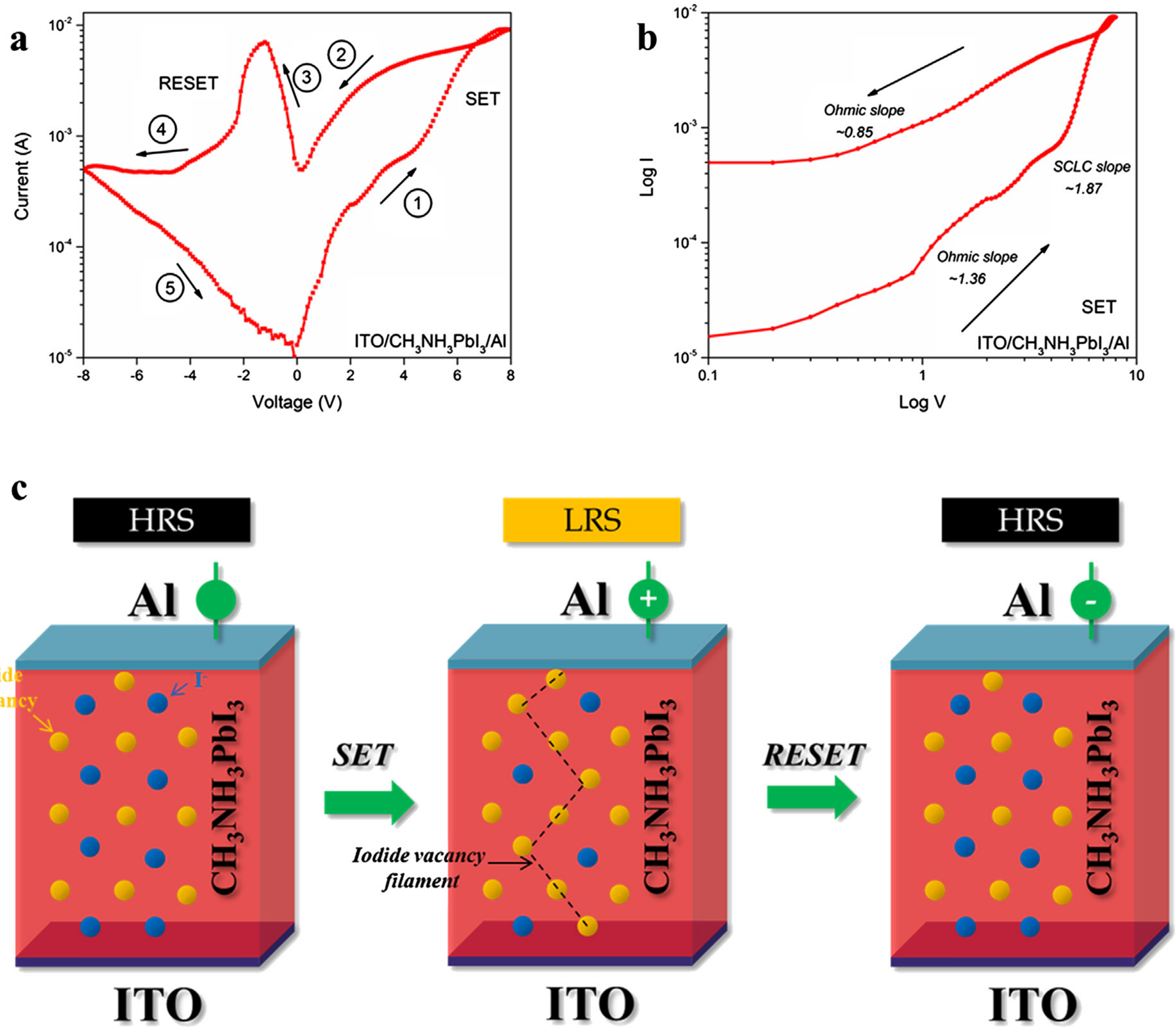

Fig. 6. (a) Semi logarithmic *I-V* curves of $CH_3NH_3PbI_3$ perovskite as ReRaM devices, (b) Log I vs Log V fitted with different conduction mechanisms of $CH_3NH_3PbI_3$ perovskite. (c) Schematic diagram of iodide vacancy filamentary conduction in ITO/$CH_3NH_3PbI_3$/Al memory device.

The mechanism for the ITO/$CH_3NH_3PbI_3$/Au WORM behaviour properties also resembles in the previously mentioned ITO/$CH_3NH_3PbI_3$/Ag structure (Fig. 7c). The charges get trapped in the trapping sites when current was swept across until all the trapping sites were filled creating a filamentary conduction pathway between ITO and the Au cathode. Therefore, the diffusion of Au into the $CH_3NH_3PbI_3$ perovskite layer is possible. Moreover, applying a negative potential across the device does not remove the Au filament pathway. Increasing the potential above operating range would damage the device instead.

3.4. Comparison of memory behaviour in ITO/$CH_3NH_3PbI_3$/Al, ITO/$CH_3NH_3PbI_3$/Ag and ITO/$CH_3NH_3PbI_3$/Au devices

The presence of non-volatile resistive switching memory behaviour can be further explained using electrochemical metallization mechanism (ECM) and valence change mechanism (VCM) [52]. Sun et al. reported that there exists a competition between iodide vacancies and the metallic filament depending on their activation or migration energies to form the filamentary conduction [54]. Based on the ITO/$CH_3NH_3PbI_3$/Al memory device, the major factor causing ReRAM characteristic lies in the VCM where it is proposed that iodide vacancies form the filamentary conduction. Although the Al atoms move towards the $CH_3NH_3PbI_3$ layer, the formation of Al metal filament is not complete to connect between the bottom and top electrodes. Through this, only the iodide vacancy filament forms the conduction filament as Al is not conductive enough to form its own filamentary conduction. The iodide vacancy filament can then be interchangeably formed and ruptured upon the direction of the sweep voltage. Hence, ReRAM memory behaviour is concluded.

On the other hand, for ITO/$CH_3NH_3PbI_3$/Ag or ITO/$CH_3NH_3PbI_3$/Au memory devices, the ECM plays a major role, where the electrochemically active electrode metals containing Ag^+ or Au^+ cations migrate towards the ITO interface and forming the metal filaments connecting both top and bottom electrodes. Although there is competition between iodide vacancies and Ag or Au atoms, the conductivity of Ag or Au filaments are shunt-wound in memory devices and are much higher than iodide vacancies [55]. Therefore, they formed the major pathway through metal filamentary conduction. When we applied a negative sweep voltage across the device, we did not observe the electrochemical dissolution of the metal filaments that implies ReRAM behaviour, but otherwise indicates WORM memory characteristics. Although we were able to increase the sweep voltage in order to observe the rupture the metal filaments back to HRS, such increase in sweep voltage especially exceeding 10 V in this project would incur high power consumption and damage over multiple cycles in the $CH_3NH_3PbI_3$ layer. Hence, our memory devices using Ag or Au electrodes shows WORM behaviour within optimum operating voltage window. This also explains why Ag and Au are favourable in forming the metal filaments over Al due to Al's lower conductivity. Such studies on these metal electrodes in observing ReRAM and WORM memory

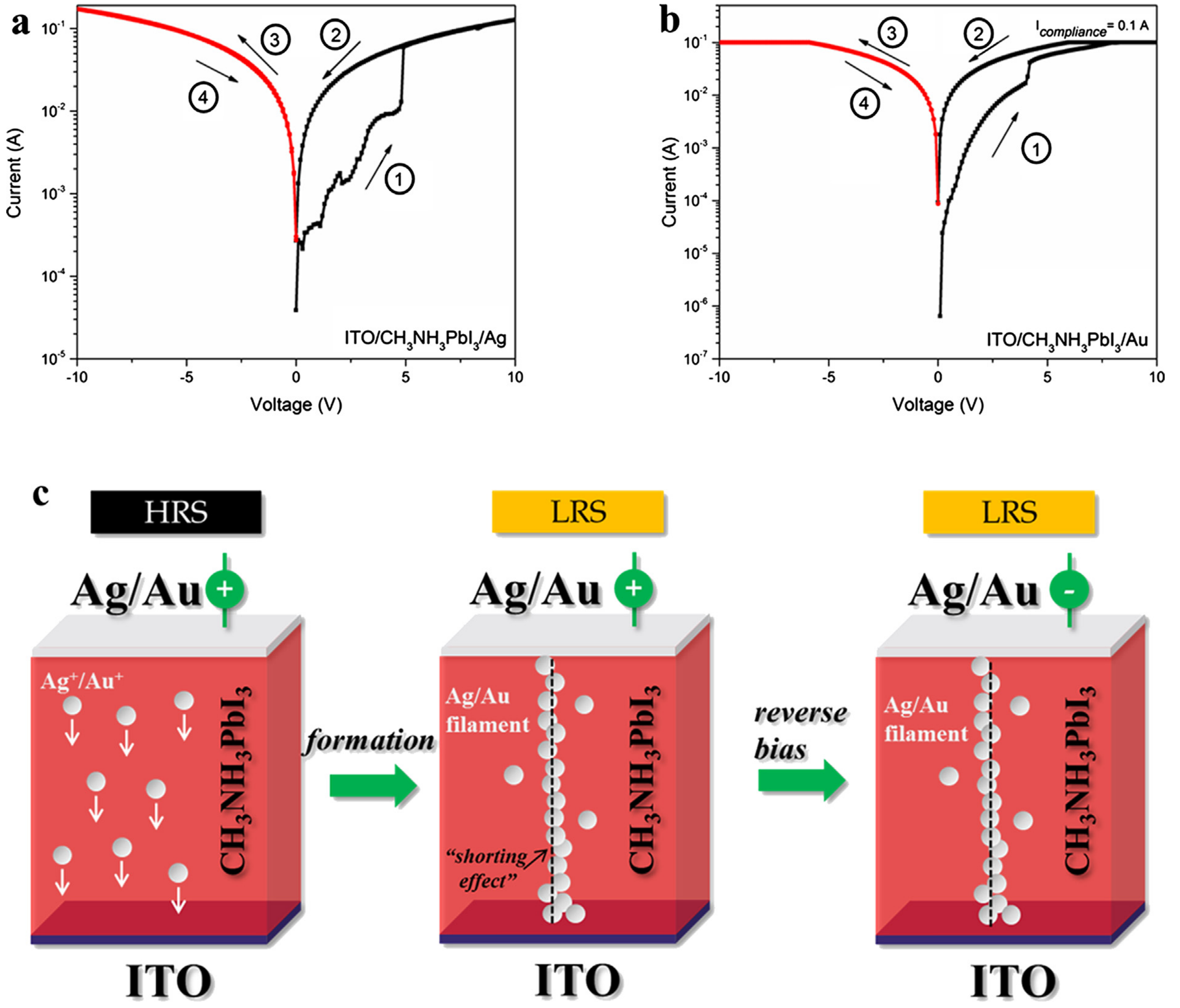

Fig. 7. (a) Semi logarithmic *I-V* curves of $CH_3NH_3PbI_3$ perovskite in ITO/ $CH_3NH_3PbI_3$/Ag, (b) ITO/ $CH_3NH_3PbI_3$/Au as WORM resistive switching devices, and (c) schematic diagram of formation of Ag or Au filament in ITO/$CH_3NH_3PbI_3$/Ag or ITO/ $CH_3NH_3PbI_3$/Au memory device.

characteristics still requires further research and understanding in applying the right electrodes for certain applications.

4. Conclusion

In conclusion, we have successfully demonstrated the various resistive switching behaviours using a simple ITO/$CH_3NH_3PbI_3$/metal memory structure device using Al, Ag, and Au. Devices with Al as cathode demonstrated ReRAM characteristics as the memory device could be SET-RESET, due to the complete formation of iodide vacancies pathway in the $CH_3NH_3PbI_3$ perovskite layer. On the other hand, devices with Ag or Au cathodes exhibited WORM behaviour in the resistive switching devices as the diffusion of Ag or Au formed metal filaments from top to bottom electrodes. Through this, the study of selecting suitable electrodes for targeted memory applications (ReRAM or WORM) can be understood and also opens up possible further research route on the metal electrodes towards commercialization of these devices.

Acknowledgements

This work was supported by University of Malaya (University Malaya Research Grant (UMRG) – AFR (Frontier Science) (RP038C-12AFR) and (FG0011-17AFR); and Postgraduate Research Grant (PPP) (PG024-2015B).

References

[1] D. Liu, M.K. Gangishetty, T.L. Kelly, Effect of $CH_3NH_3PbI_3$ thickness on device efficiency in planar heterojunction perovskite solar cells, J. Mater. Chem. A 2 (2014) 19873–19881, https://doi.org/10.1039/c4ta02637c.

[2] T. Handa, D.M. Tex, A. Shimazaki, A. Wakamiya, Y. Kanemitsu, Charge injection mechanism at heterointerfaces in $CH_3NH_3PBI_3$ perovskite solar cells revealed by simultaneous time-resolved photoluminescence and photocurrent measurements, J. Phys. Chem. Lett 8 (2017) 954–960, https://doi.org/10.1021/acs.jpclett.6b02847.

[3] T. Dittrich, F. Lang, O. Shargaieva, J. Rappich, N.H. Nickel, E. Unger, B. Rech, Diffusion length of photo-generated charge carriers in layers and powders of $CH_3NH_3PbI_3$ perovskite, Appl. Phys. Lett 109 (2016) 1–5, https://doi.org/10.1063/1.4960641.

[4] L.J. Phillips, A.M. Rashed, R.E. Treharne, J. Kay, P. Yates, I.Z. Mitrovic, A. Weerakkody, S. Hall, K. Durose, Maximizing the optical performance of planar $CH_3NH_3PbI_3$ hybrid perovskite heterojunction stacks, Sol. Energy Mater. Sol. Cells 147 (2016) 327–333, https://doi.org/10.1016/j.solmat.2015.10.007.

[5] Y. A, B. M, B. X, W. J, Z. W, Investigation of optical and dielectric constants of organic-inorganic $CH_3NH_3PbI_3$ perovskite thin films, J. Nanomed. Nanotechnol. 07 (2016) 5–9, https://doi.org/10.4172/2157-7439.1000407.

[6] T. Shi, Q. Teng, X.B. Yang, H.L. Yip, Y.J. Zhao, The electronic properties of $CH_3NH_3PbI_3$ perovskite surfaces tuned by inverted polarities of pyridine and ethylamine, J. Mater. Chem. C 6 (2018) 6733–6738, https://doi.org/10.1039/c8tc00409a.

[7] J. Haruyama, K. Sodeyama, L. Han, Y. Tateyama, Surface properties of $CH_3NH_3PbI_3$ for perovskite solar cells, Acc. Chem. Res. 49 (2016) 554–561, https://doi.org/10.1021/acs.accounts.5b00452.

[8] J. Troughton, K. Hooper, T.M. Watson, Humidity resistant fabrication of $CH_3NH_3PbI_3$ perovskite solar cells and modules, Nano Energy 39 (2017) 60–68,

https://doi.org/10.1016/j.nanoen.2017.06.039.

[9] J. Zheng, M. Zhang, C.F.J. Lau, X. Deng, J. Kim, Q. Ma, C. Chen, M.A. Green, S. Huang, A.W.Y. Ho-Baillie, Spin-coating free fabrication for highly efficient perovskite solar cells, Sol. Energy Mater. Sol. Cells 168 (2017) 165–171, https://doi.org/10.1016/j.solmat.2017.04.029.

[10] X. Zeng, T. Zhou, C. Leng, Z. Zang, M. Wang, W. Hu, X. Tang, S. Lu, L. Fang, M. Zhou, Performance improvement of perovskite solar cells by employing a CdSe quantum dot/PCBM composite as an electron transport layer, J. Mater. Chem. A. 5 (2017) 17499–17505, https://doi.org/10.1039/C7TA00203C.

[11] M. Wang, Z. Zang, B. Yang, X. Hu, K. Sun, L. Sun, Performance improvement of perovskite solar cells through enhanced hole extraction: The role of iodide concentration gradient, Sol. Energy Mater. Sol. Cells 185 (2018) 117–123, https://doi.org/10.1016/j.solmat.2018.05.025.

[12] S. Tong, H. Wu, C. Zhang, S. Li, C. Wang, J. Shen, S. Xiao, J. He, J. Yang, J. Sun, Y. Gao, Large-area and high-performance $CH_3NH_3PbI_3$ perovskite photodetectors fabricated via doctor blading in ambient condition, Org. Electron. Physics, Mater. Appl. 49 (2017) 347–354, https://doi.org/10.1016/j.orgel.2017.07.011.

[13] Y. Wang, Q. Song, T. Lin, Y. Fu, X. Sun, B. Chu, F. Jin, H. Zhao, W. Li, Z. Su, Y. Li, Improved performance of $CH_3NH_3PbI_3$ based photodetector with a MoO_3 interface layer, Org. Electron. Physics, Mater. Appl. 49 (2017) 355–359, https://doi.org/10.1016/j.orgel.2017.07.013.

[14] S. Li, S. Tong, J.Q. Meng, C. Zhang, C. Zhang, J. Shen, S. Xiao, J. Sun, J. He, Y. Gao, B. Yang, J. Yang, Fast-response and high-responsivity $FA_xMA_{(1-x)}PbI_3$ photodetectors fabricated via doctor-blading deposition in ambient condition, Org. Electron. Physics, Mater. Appl. 52 (2018) 190–194, https://doi.org/10.1016/j.orgel.2017.10.024.

[15] J. Xu, Y. Chen, L. Dai, Efficiently photo-charging lithium-ion battery by perovskite solar cell, Nat. Commun. 6 (2015) 1–7, https://doi.org/10.1038/ncomms9103.

[16] M. Wang, Y. Shi, J. Bian, Q. Dong, H. Sun, H. Liu, Y. Luo, Y. Zhang, Electroluminescence from perovskite LEDs with the structure of Ag/Spiro-OMeTAD/ $CH_3NH_3PbI_3/TiO_2$/FTO, Chem. Phys. Lett. 662 (2016) 176–181, https://doi.org/10.1016/j.cplett.2016.09.041.

[17] L. Cheng, Y. Cao, R. Ge, Y.Q. Wei, N.N. Wang, J.P. Wang, W. Huang, Sky-blue perovskite light-emitting diodes based on quasi-two-dimensional layered perovskites, Chinese Chem. Lett. 28 (2017) 29–31, https://doi.org/10.1016/j.cclet.2016.07.001.

[18] H. Cai, G. Ma, Y. He, C. Liu, H. Wang, A remarkable performance of $CH_3NH_3PbI_3$ perovskite memory based on passivated method, Org. Electron. Physics, Mater. Appl. 58 (2018) 301–305, https://doi.org/10.1016/j.orgel.2018.04.025.

[19] Y. Liu, F. Li, Z. Chen, T. Guo, C. Wu, T.W. Kim, Resistive switching memory based on organic/inorganic hybrid perovskite materials, Vacuum. 130 (2016) 109–112, https://doi.org/10.1016/j.vacuum.2016.05.010.

[20] H. Liu, Y. Wu, Y. Hu, Reproducible switching effect of an all-inorganic halide perovskite CsPbBr 3 for memory applications, Ceram. Int. 43 (2017) 7020–7025, https://doi.org/10.1016/j.ceramint.2017.02.128.

[21] J.H. Heo, D.H. Shin, S.H. Moon, M.H. Lee, D.H. Kim, S.H. Oh, W. Jo, S.H. Im, Memory effect behavior with respect to the crystal grain size in the organic-inorganic hybrid perovskite nonvolatile resistive random access memory, Sci. Rep. 7 (2017) 1–8, https://doi.org/10.1038/s41598-017-16805-4.

[22] C. Gu, J.S. Lee, Flexible hybrid organic-inorganic perovskite memory, ACS Nano. 10 (2016) 5413–5418, https://doi.org/10.1021/acsnano.6b01643.

[23] T. Guo, B. Sun, S. Mao, S. Zhu, Y. Xia, H. Wang, Y. Zhao, Z. Yu, A resistance ratio change phenomenon observed in Al doped ZnO (AZO)/$Cu_{(In1\text{-}xGax)}Se_2$/Mo resistive switching memory device, Appl. Surf. Sci. 433 (2018) 535–539, https://doi.org/10.1016/j.apsusc.2017.10.073.

[24] A. Chiappone, M. Gillono, M. Castellino, K. Bejtka, K. Rajan, I. Roppolo, D. Perrone, S. Bocchini, C. Ricciardi, C.F. Pirri, A. Chiolerio, In situ generation of silver nanoparticles in PVDF for the development of resistive switching devices, Appl. Surf. Sci. 455 (2018) 418–424, https://doi.org/10.1016/j.apsusc.2018.06.001.

[25] T.J. Whitcher, K.L. Woon, W.S. Wong, N. Chanlek, H. Nakajima, T. Saisopa, P. Songsiriritthigul, Interfacial behavior of resistive switching in ITO-PVK-Al WORM memory devices, J. Phys. D. Appl. Phys. 49 (2016), https://doi.org/10.1088/0022-3727/49/7/075104.

[26] C. Wang, Y. Chen, B. Zhang, S. Liu, Q. Chen, Y. Cao, S. Sun, High-efficiency bulk heterojunction memory devices fabricated using organometallic halide perovskite:poly(N-vinylcarbazole) blend active layers, Dalt. Trans. 45 (2015) 484–488, https://doi.org/10.1039/c5dt03969j.

[27] X.-F. Cheng, X. Hou, J. Zhou, B.-J. Gao, J.-H. He, H. Li, Q.-F. Xu, N.-J. Li, D.-Y. Chen, J.-M. Lu, Pseudohalide-induced 2D $(CH_3NH_3)_2PbI_2(SCN)_2$ perovskite for ternary resistive memory with high performance, Small 1703667 (2018) 1703667, https://doi.org/10.1002/smll.201703667.

[28] X. Zhu, H. Sun, D. Yang, J. Yang, X. Li, X. Gao, Fabrication and characterization of X-ray array detectors based on polycrystalline PbI2thick films, J. Mater. Sci. Mater. Electron. 25 (2014) 3337–3343, https://doi.org/10.1007/s10854-014-2023-y.

[29] Y. Li, W. Yan, Y. Li, S. Wang, W. Wang, Z. Bian, L. Xiao, Q. Gong, Direct observation of long electron-hole diffusion distance in $CH_3NH_3PbI_3$ perovskite thin film, Sci. Rep. 5 (2015) 1–8, https://doi.org/10.1038/srep14485.

[30] S.M. Jain, B. Philippe, E.M.J. Johansson, B. Park, H. Rensmo, T. Edvinsson, G. Boschloo, Vapor phase conversion of PbI2 to CH3NH3PbI3: spectroscopic evidence for formation of an intermediate phase, J. Mater. Chem. A. 4 (2016) 2630–2642, https://doi.org/10.1039/C5TA08745G.

[31] Y. Zhao, K. Zhu, Three-step sequential solution deposition of PbI_2-free $CH_3NH_3PbI_3$ perovskite, J. Mater. Chem. A. 3 (2015) 9086–9091, https://doi.org/10.1039/c4ta05384b.

[32] J.J. Zhao, P. Wang, Z.H. Liu, L.Y. Wei, Z. Yang, H.R. Chen, X.Q. Fang, X.L. Liu, Y.H. Mai, Controlled reaction for improved $CH_3NH_3PbI_3$ transition in perovskite solar cells, Dalt. Trans. 44 (2015) 17841–17849, https://doi.org/10.1039/c5dt02587g.

[33] D. Bi, S.-J. Moon, L. Häggman, G. Boschloo, L. Yang, E.M.J. Johansson, M.K. Nazeeruddin, M. Grätzel, A. Hagfeldt, Using a two-step deposition technique to prepare perovskite ($CH_3NH_3PbI_3$) for thin film solar cells based on ZrO_2 and TiO_2 mesostructures, RSC Adv. 3 (2013) 18762, https://doi.org/10.1039/c3ra43228a.

[34] F. Jia, Y. Guo, L. Che, Z. Liu, Z. Zeng, C. Cai, Synergic solventing-out crystallization with subsequent time-delay thermal annealing of PbI_2 precursor in mesostructured perovskite solar cells, Mater. Res. Exp. 5 (2018) 066404, , https://doi.org/10.1088/2053-1591/aabe13.

[35] S.A. Kulkarni, T. Baikie, P.P. Boix, N. Yantara, N. Mathews, S. Mhaisalkar, Band-gap tuning of lead halide perovskites using a sequential deposition process, J. Mater. Chem. A. 2 (2014) 9221–9225, https://doi.org/10.1039/c4ta00435c.

[36] Y. Gao, Light-Induced Degradation of CH3NH3PbI3 Hybrid Perovskite Thin Film, (2017) 6–12. http://doi.org/10.1021/acs.jpcc.6b11853.

[37] W. Fangyan, X. Yongli, Degradation of co-evaporated perovskite thin film in air, Chem. Phys. Lett. (2015), https://doi.org/10.1016/j.cplett.2015.12.046.

[38] C. Rocks, V. Svrcek, P. Maguire, D. Mariotti, Understanding surface chemistry during $MAPbI_3$ spray deposition and its effect on photovoltaic performance, J. Mater. Chem. C 5 (2017) 902–916, https://doi.org/10.1039/C6TC04864A.

[39] Y. Wang, W.Y. Rho, H.Y. Yang, T. Mahmoudi, S. Seo, D.H. Lee, Y.B. Hahn, Air-stable, hole-conductor-free high photocurrent perovskite solar cells with $CH_3NH_3PbI_3$–NiO nanoparticles composite, Nano Energy 27 (2016) 535–544, https://doi.org/10.1016/j.nanoen.2016.08.006.

[40] B. Philippe, B.W. Park, R. Lindblad, J. Oscarsson, S. Ahmadi, E.M.J. Johansson, H. Rensmo, Chemical and electronic structure characterization of lead halide perovskites and stability behavior under different exposures-A photoelectron spectroscopy investigation, Chem. Mater. 27 (2015) 1720–1731, https://doi.org/10.1021/acs.chemmater.5b00348.

[41] Y. Zhao, A.M. Nardes, K. Zhu, Mesoporous perovskite solar cells: Material composition, charge-carrier dynamics, and device characteristics, Faraday Discuss. 176 (2014) 301–312, https://doi.org/10.1039/c4fd00128a.

[42] L.C. Chen, J.C. Chen, C.C. Chen, C.G. Wu, Fabrication and properties of high-efficiency perovskite/PCBM organic solar cells, Nanoscale Res. Lett. 10 (2015) 2–6, https://doi.org/10.1186/s11671-015-1020-2.

[43] P.S. Shinde, G.H. Go, W.J. Lee, Facile growth of hierarchical hematite (α-Fe_2O_3) nanopetals on FTO by pulse reverse electrodeposition for photoelectrochemical water splitting, J. Mater. Chem. 22 (2012) 10469–10471, https://doi.org/10.1039/c2jm31254a.

[44] M.I. Saidaminov, A.L. Abdelhady, B. Murali, E. Alarousu, V.M. Burlakov, W. Peng, I. Dursun, L. Wang, Y. He, G. MacUlan, A. Goriely, T. Wu, O.F. Mohammed, O.M. Bakr, High-quality bulk hybrid perovskite single crystals within minutes by inverse temperature crystallization, Nat. Commun. 6 (2015) 1–6, https://doi.org/10.1038/ncomms8586.

[45] A. Calloni, A. Abate, G. Bussetti, G. Berti, R. Yivlialin, F. Ciccacci, L. Duò, Stability of organic cations in solution-processed $CH_3NH_3PbI_3$ perovskites: formation of modified surface layers, J. Phys. Chem. C. 119 (2015) 21329–21335, https://doi.org/10.1021/acs.jpcc.5b05422.

[46] H.S. Kim, C.R. Lee, J.H. Im, K.B. Lee, T. Moehl, A. Marchioro, S.J. Moon, R. Humphry-Baker, J.H. Yum, J.E. Moser, M. Grätzel, N.G. Park, Lead iodide perovskite sensitized all-solid-state submicron thin film mesoscopic solar cell with efficiency exceeding 9%, Sci. Rep. 2 (2012), https://doi.org/10.1038/srep00591.

[47] M. Zubair, M. Mustafa, A. Ali, Y.H. Doh, K.H. Choi, Improvement of solution based conjugate polymer organic light emitting diode by ZnO–graphene quantum dots, J. Mater. Sci. Mater. Electron. 26 (2015) 3344–3351, https://doi.org/10.1007/s10854-015-2837-2.

[48] Y. Wang, Z. Lv, L. Zhou, X. Chen, J. Chen, Y. Zhou, V.A.L. Roy, S.T. Han, Emerging perovskite materials for high density data storage and artificial synapses, J. Mater. Chem. C. 6 (2018) 1600–1617, https://doi.org/10.1039/c7tc05326f.

[49] E. Lim, R. Ismail, Conduction mechanism of valence change resistive switching memory: a survey, Electronics 4 (2015) 586–613, https://doi.org/10.3390/electronics4030586.

[50] D. Shi, V. Adinolfi, R. Comin, M. Yuan, E. Alarousu, A. Buin, Y. Chen, S. Hoogland, A. Rothenberger, K. Katsiev, Y. Losovyj, X. Zhang, P.A. Dowben, O.F. Mohammed, E.H. Sargent, O.M. Bakr, Low trap-state density and long carrier diffusion in organolead trihalide perovskite, Single Crystals, Sci. (80-.) 347 (2015) 519–522, https://doi.org/10.1126/science.aaa2725.

[51] A. Walsh, D.O. Scanlon, S. Chen, X.G. Gong, S.H. Wei, Self-regulation mechanism for charged point defects in hybrid halide perovskites, Angew. Chemie - Int. Ed. 54 (2015) 1791–1794, https://doi.org/10.1002/anie.201409740.

[52] D. Barboni, R.A. De Souza, The thermodynamics and kinetics of iodine vacancies in the hybrid perovskite methylammonium lead iodide, Energy Environ. Sci. (2018), https://doi.org/10.1039/C8EE01697F.

[53] J.M. Azpiroz, E. Mosconi, J. Bisquert, F. De Angelis, Defect migration in methylammonium lead iodide and its role in perovskite solar cell operation, Energy Environ. Sci. 8 (2015) 2118–2127, https://doi.org/10.1039/c5ee01265a.

[54] Y. Sun, M. Tai, C. Song, Z. Wang, J. Yin, Competition between metallic and vacancy defect conductive filaments in a $CH_3NH_3PbI_3$-based memory device, J. Phys. Chem. C. 122 (2018) 6431–6436, https://doi.org/10.1021/acs.jpcc.7b12817.

[55] Y. Sun, C. Song, J. Yin, X. Chen, Q. Wan, F. Zeng, F. Pan, Guiding the growth of a conductive filament by nanoindentation to improve resistive switching, ACS Appl. Mater. Interf. 9 (2017) 34064–34070, https://doi.org/10.1021/acsami.7b09710.